Metal-organic framework (MOF) dispersion based fluids for solar-thermal energy conversion

Solar Energy 273 (2024) 112542

Contents lists available at ScienceDirect

Solar Energy

journal homepage: www.elsevier.com/locate/solener

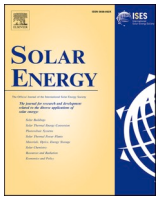

Metal-organic framework (MOF) dispersion based fluids for solar-thermal energy conversion

Hussein Sayed Moghaieb, Sameh Khalil, Abhijit Ganguly, Paul Maguire, Davide Mariotti, Supriya Chakrabarti *

School of Engineering, Ulster University, York St, Belfast BT15 1AP, UK

ARTICLE INFO

Keywords:
Metal-organic framework (MOF)
MOF dispersion
Solar-thermal energy conversion (STEC)
Heat transfer fluid (HTFs)
Porous structure nanofluid
Solar harvesting

ABSTRACT

This paper discusses the potential use of metal–organic framework (MOF) dispersion based fluids for solar-to-thermal energy conversion (STEC). For this, the optical and thermal characteristics of MOF dispersion were investigated, with MOFs dispersed in ethylene glycol (EG). This study is focused on three different MOF dispersions, namely ZIF8/EG, CuBTC/EG, and FeBTC/EG, each with varying concentrations of MOF particles. The results showed that FeBTC/EG at a concentration of 0.3 wt% is the optimal fluid for STEC, exhibiting the highest absorption and STEC efficiency compared to the other two fluids. The study also highlights the trade-off between STEC efficiency and cost, as increasing the concentration of MOF particles decreases the specific absorption rate (SAR). Additionally, the paper evaluates the dispersion stability of FeBTC/EG over time, which is critical for practical STEC applications. The novelty of the paper lies in the use of MOF dispersion based fluids for STEC application, which has not been extensively studied before. This study provides valuable insights into the potential use of MOF/EG for STEC and highlights the importance of optimizing the concentration of MOF particles for efficient and cost-effective performance. This study also introduces the novel application of MOF dispersion based fluids for enhanced STEC performance, showcasing FeBTC/EG as a standout for its high efficiency and stability. It marks a significant stride in utilizing MOF materials for sustainable energy, emphasizing practical considerations of dispersion stability and cost-effectiveness in STEC systems.

1. Introduction

Due to the anticipated depletion of fossil fuels and their adverse impacts on the environment, the world is currently seeking alternative solutions to meet the rising energy demands. Among a variety of resources, solar energy has gained increasing interest since it is clean, abundant, and renewable [1–3]. Using solar collectors to capture solar energy and convert it into thermal energy is one of the most efficient ways to utilize solar energy [4]. Conventional solar collectors conduct the solar-to-thermal energy conversion (STEC) process employing selective solid materials, and the heat generated is subsequently transferred to conventional heat transfer fluids (HTFs), including water, glycols, and thermal oils. These solar collector devices, however, faced two major downsides. First, the high temperature of the surface absorber increases the heat loss, resulting in poor performance as well as material degradation over time [5]. Second, because of their comparatively low thermal conductivity, the traditional HTFs used in these systems showed poor thermal transport [6]. Alternatively, the concept of direct absorption solar collectors (DASCs) was introduced in which the HTF is exposed directly to the solar radiation without the need for solid surface absorbers [7]. This, however, requires the working fluid to have high solar absorption properties, which can't be accomplished by conventional HTFs, since they are transparent in the visible region, which makes up approximately half of the solar energy received at the earth surface at air mass of 1.5 (AM1.5) [8].

Alternatively, fluids with dispersed nano/micro particles were introduced as a novel solution to overcome such limitations of conventional HTFs and offer superior optical and thermal properties [6,9]. These particles can be made from various materials, such as metals, metal oxides, or carbon-based materials [10–13], and are typically dispersed in a base fluid, such as water, oil, or ethylene glycol [11]. Adding nano/micro solid particles to conventional fluids results in unique thermal and physical properties that differ from those of the base fluid, such as higher thermal conductivity, increased convective heat

* Corresponding author.
E-mail address: s.chakrabarti@ulster.ac.uk (S. Chakrabarti).

https://doi.org/10.1016/j.solener.2024.112542
Received 4 January 2024; Received in revised form 21 March 2024; Accepted 12 April 2024
Available online 18 April 2024

transfer, and improved stability [8,11]. These properties make them attractive for use in a wide range of applications, including electronic cooling, automotive cooling, and solar-to-thermal energy conversion [4–6]. However, the conventional small particles suffer from various drawbacks like restricted light absorption spectrum, low dispersion stability, easy agglomeration, poor chemical, and thermal stability in base fluid [14–16]. Also, the broadband and high intensity absorption specific to STEC are unlikely to be met with existing/commercially available small particles. The search for a new class of materials is thus necessary. Here we have introduced a new class of porous structured metal organic framework (MOF) materials with high surface area for STEC application. These porous structures can enhance light absorption capability of materials by reducing light reflection due to the reduced effective refractive index of the materials and minimized angular dependence of the incident light [13,17]. Moreover, the pores serve as optical microcavities for light confinement through multiple light reflection and scattering, which greatly enhance the light–material interaction [18–22]. These properties make MOF dispersion based fluids attractive for use in a wide range of STEC applications. The selection of the three MOFs used in this work — ZIF8, CuBTC, and FeBTC —was guided by a set of criteria designed to optimize STEC efficiency. These criteria encompassed the optical and thermal properties of the MOFs [23], which are crucial for enhanced optical absorption and thermal characteristics in STEC applications. The study also assessed the dispersion stability of these MOF/EG over time, an essential factor for their practical application in STEC systems. Material availability was another key consideration; the chosen MOFs were readily available and represented a variety of metal bases (copper, iron, and zinc), offering a broad perspective on performance differences across different metal centres. Environmental impact and sustainability were also considered, aligning with the goal of finding alternatives to conventional HTFs. Lastly, the innovative potential of using MOF dispersion based fluids in STEC systems significantly influenced their selection, as this application has not been extensively explored previously.

2. Experimental details

2.1. Materials and preparation of MOF dispersion based fluids

In this work, three types of MOFs were utilized, each uniquely based on a different metal such as copper (CuBTC), iron (FeBTC) and zinc (ZIF8). The three MOF materials were purchased from Sigma-Aldrich specifically under the product names Basolite® C300 for CuBTC, Basolite® F300 for FeBTC and Basolite® Z1200 for ZIF8. Each MOF has a unique empirical formula and molecular weight, see *Supporting Information*, Table S1. To prepare the MOF dispersion, each MOF powder was precisely weighed using a microscale and then transferred into a glass vial (see Fig. S1 in *Supporting Information*, Section 1). Ethylene glycol (EG), selected as the dispersion medium and was added to the powder in the vial for dispersion at a mass concentration of 0.3 wt%. EG was selected as our base fluid over water or thermal oils due to its broader operating temperature range and enhanced chemical stability, which facilitates superior dispersion of MOFs [8]. Additionally, EG is well-regarded for commercial use because of its broad operational temperature range, making it a pragmatic choice for this study. A two-step dispersion process for each MOF was carried out using a bath-type sonicator (VWR USC300TH, 230 V, 50 Hz, 370VA) employed for 2 h, followed by a probe-type sonicator (VCX-130 PB ultrasonic processor, Sonics Materials) for 3 min at 80 % (104 W). This dispersion procedure was meticulously replicated for each type of MOF powder under identical conditions (see Fig. S2). After preparation, each MOF/EG sample was further diluted to give a lower mass concentration of 0.1 wt%. Following, the optical properties and STEC performance of the MOF/EG were characterized and analysed as presented in the subsequent sections of this work. The choice of this range of concentrations is based on both prevalent practices in existing literature and our own prior experiments with such dispersion based fluids.

2.2. Characterizations of MOF and MOF dispersion based fluids

Prior to any basic material characterizations, the MOF powders were well-dispersed in ethanol (EtOH) under ultrasonication, maintaining the material's concentration around 1 mg/ml for all three MOFs. Next, the respective solutions were drop-casted onto a clean Si wafer and allowed to dry under infrared radiation for the characterization using Field-emission scanning electron microscopy (FE-SEM), energy-dispersive X-ray microanalysis (EDX), X-ray diffraction (XRD), Raman Spectroscopy and X-ray photoelectron spectroscopy (XPS).

Surface morphologies were studied by using FE-SEM (Hitachi SU5000, Japan), which is coupled with energy-dispersive X-ray microanalysis (EDX) for the analysis of elemental composition. EDX elemental spectra and mapping were performed using the X-Max^N 80 mm^2 silicon drift detector (Oxford Instruments) coupled with FE-SEM at 10 kV operating voltage and data was collected using AZtec software (Oxford Instruments). XRD study was carried out to determine the crystalline structure using a Malvern Panalytical Empyrean-3, operated in reflection mode at 45 kV voltage and 40 mA current, with Cu Kα radiation ($\lambda = 1.54$ Å). Raman spectroscopy was used to obtain experimental information about the electronic and vibrational properties of the samples. The Raman data was collected by using an excitation wavelength of 532 nm (RL532C laser source) at a Renishaw Invia Qontor system. The surface chemical composition and phase identification were carried out by XPS an ESCALAB Xi$^+$ spectrometer microprobe (Thermo Fisher Scientific) with a focussed monochromatic Al Kα ($h\nu = 1486.6$ eV, 650 μm spot size) operating at a power of 225 W (15 kV and 15 mA). The operating pressure of the system was maintained at 10^{-9} bar, which increased up to 10^{-7} bar with charge neutraliser (flood gun) operated at 100 mA emission current. Elemental composition of surface of the samples were analysed using the CasaXPS software with Shirley background corrected baseline with Kratos library relative sensitivity factors (RSF). The binding energies were calibrated for specimen charging by referencing C 1 s to 284.5 eV.

Optical properties of the MOF dispersion based fluids were measured using ultraviolet–visible-near infrared (UV–Vis-NIR) spectroscopy with an integrating sphere (LAMBDA 1050 +, PerkinElmer Inc.) over a wavelength range from 300 to 1500 nm. For the transmittance measurements an empty cuvette was used as reference as this approach allows for a direct comparison between the transmittance of EG and the MOF/EG with limited errors. To evaluate the absorption and scattering coefficients, the MOF/EG, loading into a quartz cuvette (3.5 mL capacity and 1 cm light path length, PerkinElmer Inc, see Fig. S2), was placed in the transmission port to measure its transmittance signal, and then centrally mounted in the integrating sphere to measure combined signals of transmittance and scattering. More details are provided in the *Supporting Information* (Section 2) with regard to the principle of measurements [24–26] (See Fig. S3) and the calculations of the absorption (μ_a, Equation S13) and scattering coefficients (μ_s, Equation S14).

2.3. Solar-thermal energy conversion (STEC) experiment

As illustrated in Fig. 1, to evaluate the STEC performance of the MOF/EG, it was exposed to a solar light simulator (LS0106, 150-W Xenon lamp, Quantum Design Inc.), which provides a uniform collimated beam of 25 mm diameter at a constant intensity of ~ 1000 W/m^2 (one sun). Prior to conducting the experiments, a sample volume of 1 mL of each MOF/EG was loaded into a petri dish fabricated from quartz with inner and outer diameters of 19 mm and 23.4 mm, respectively, a height of 9.1 mm, and a bottom thickness of 2.5 mm. Such a small sample volume of 1 mL was used to maintain a sufficiently uniform temperature distribution within the MOF/EG during exposure to light. After loading each MOF/EG, the quartz petri dish was covered with a disc of the same material with a thickness of 1.5 mm. The petri dish and cover were

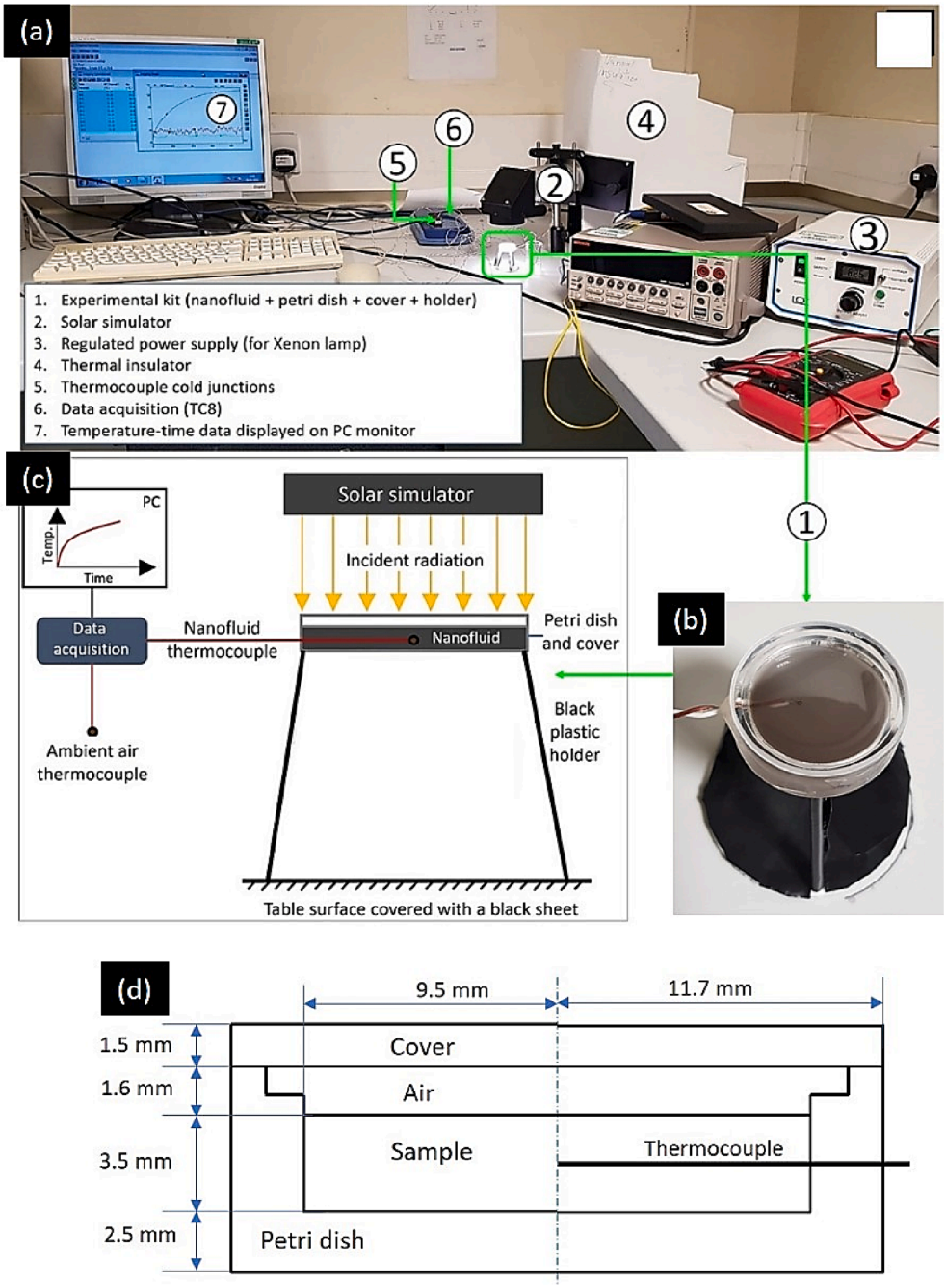

Fig. 1. STEC experimental setup of MOF/EG. (b) Experimental STEC kit consists of the covered petri dish containing one of the MOF/EG and mounted on a plastic holder with the thermocouple junction shown, as all illustrated by a schematic diagram in (c). (d) Kit geometry and materials used with all dimensions are defined., . adapted from our previous publication [25]

designed so that a still air layer of ~ 2 mm is trapped between the MOF/EG surface and the top cover, minimising heat loss. To record the change in temperature of this dispersion over time while being exposed to light, two T-type thermocouples were installed: one at the centre of the MOF/EG layer and the second one was hung in the air for measuring the ambient temperature. For more accuracy, the petri dish was held on a three-legged plastic support for no contact between the petri dish bottom and the table surface where experiments were performed, which eliminated heat loss by conduction. The holder was also attached to a base of a black sheet so that any light transmitted from the MOF/EG through the transparent petri dish bottom can be absorbed, preventing being reflected to the MOF/EG, which could result in overestimating the STEC efficiency. The black sheet (shown in Fig. 1b and Fig. S4) is an in-house fabricated film of carbon nanotubes (CNT), known for their exceptional solar absorption capabilities and minimal light reflection. From our measurements we found that across the visible and near-infrared (NIR) spectral bands the CNT film behaves quite similarly to an ideal black body, absorbing most of the light (~99.8 %) with negligible reflectance (<0.2 %) and transmittance (<0.1 % at only 3 μm thickness), see Fig. S5 in the *Supporting Information*, Section 3, for more details about the properties of the CNT film. In addition, the petri dish was not thermally insulated to keep the STEC process unaffected by thermal and light interactions that could be imposed by the thermal insulation. The experimental kit was then coaxially positioned below the simulator output at a vertical working distance of 3 cm and the temperature was monitored until thermal equilibrium with the room

temperature was reached. The solar simulator was then turned on and the change in the temperature of the MOF/EG was continuously recorded until it reached another thermal equilibrium, at which the rate of heat generated within the MOF/EG is equal to the rate of heat loss [25,26].

An energy balance was made for calculating the experimental STEC efficiency (η_{sth}) of each MOF/EG, as well as the base fluid EG [25], as presented in Equation 1.The incident radiation (I_i) normal to the sample irradiated surface area (A_s) is attenuated by absorption and scattering within the MOF/EG volume,as the absorption process results in heat generation (q_g). In addition, reflection loss at the cover-air interface and the absorption within the glass cover were considered and subtracted from the irradiation supplied by the simulator.

$$\eta_{sth} = \frac{q_g}{I_i A_s} \tag{1}$$

The heat generated (q_g) from the STEC process can be calculated from the measured temperature rise of the MOF/EG (ΔT_{nf}) during the irradiation time (Δt) at a given heat capacity (mC_p) with taking into account the heat loss to ambient air and surroundings (q_l):

$$q_g = \frac{mC_p \Delta T}{\Delta t} + q_l \tag{2}$$

Moreover, *SAR*, which indicates how effective a unit mass of the particles in converting light into heat, can be calculated from Equation (3), where $mc_{p_{bf}}$ and $mc_{p_{np}}$ are the heat capacities and ΔT_{nf} and ΔT_{bf} are the temperature rises of EG and the dispersed particles, respectively [27].

$$SAR = \frac{\left(mc_{p_{bf}} + mc_{p_{np}}\right)\Delta T_{nf} - mc_{p_{bf}} \Delta T_{bf}}{1000 m_{np} \times \Delta t} \tag{3}$$

With neglecting m_{np} which is very small comparing with the total mass of the sample and assuming that $\Delta T_{nf} = \Delta T_{bf}$ under low irradiation as in this work, Equation (3) can be simplified as follows:

$$SAR = \frac{m_{bf} c_{bf}}{1000 m_{np}} \left(\frac{T_{nf} - T_{bf}}{\Delta t}\right) \tag{4}$$

3. Results and discussion

3.1. Characterizations of MOF

The surface morphology was studied using FE-SEM and the images are presented in Fig. 2. The analysis of these images revealed that CuBTC particles have an average size of 10–50 μm, (Fig. 2(a–b)). The CuBTC particles were found to have cubic crystalline shapes with octahedral geometry. The EDX study on CuBTC powder revealed the existence of Cu, C and O elements, as shown in the spectrum (Fig. S6a, Section 4, *Supporting Information*) and the elemental mapping (Fig. S7a). Essentially, the CuBTC particles were found to possess a high content of C and O elements compared to the Cu element because of the high content of graphitic structures present in the MOF structure that generated with two Cu atoms (in each metal corners) coordinated with four O atoms from benzene-1,3,5-tricarboxylate (BTC) linker [28,29]. Notably, a similar phenomenon is observed for all the MOFs used here (Figs. S6 and S7, Section 4, *Supporting Information*). FeBTC particles show spherical morphology and aggregation of particles, as shown in Fig. 2(c–d). The particle sizes of FeBTC varied in the range of 45 to 200 nm. As observed from the EDX spectrum (Fig. S6b) and the corresponding elemental mapping (Fig. S7b), the FeBTC particles mainly consist of three elements of Fe, C and O. As shown in Fig. 2(e–f), ZIF8 particles exhibit a typical rhombic dodecahedron crystalline morphology, and the average particle size of about 200 − 500 nm. Fig. S6c shows a representative EDX spectrum of the ZIF8 sample and the corresponding elemental mapping in Fig. S7c, indicating the presence of four elements: Zn, O, C, and N.

Fig. 3(a–c) revealed the crystalline structures of CuBTC, FeBTC and ZIF8, respectively, by using X-ray diffraction (XRD) patterns. The CuBTC exhibited high crystalline nature displaying sharp and well-defined XRD peaks (Fig. 3a), consistent with ICDD#00–062-1028 crystallographic file and reported literature [28–31]. As observed in Fig. 3a, the main diffraction peaks are found at 6.6°, 9.3°, 11.7°, 14.6°, 16.4°, 17.3°, 18.9°, 20.2°, 23.3°, 24.1°, 26.0° and 28.9°, which could be assigned to (200), (220), (222), (331), (422), (333), (440), (442), (444), (551), (553) and (660) crystal planes of cubic structure of CuBTC respectively [28]. As shown in Fig. 3b, the diffraction pattern for FeBTC MOF particles do not have strong Bragg scattering, which is quite different from the other two MOF samples. The low-resolution XRD pattern with weak and broad peaks, at 2θ = 11°, 19°, 24° and 28°, is the characteristics of

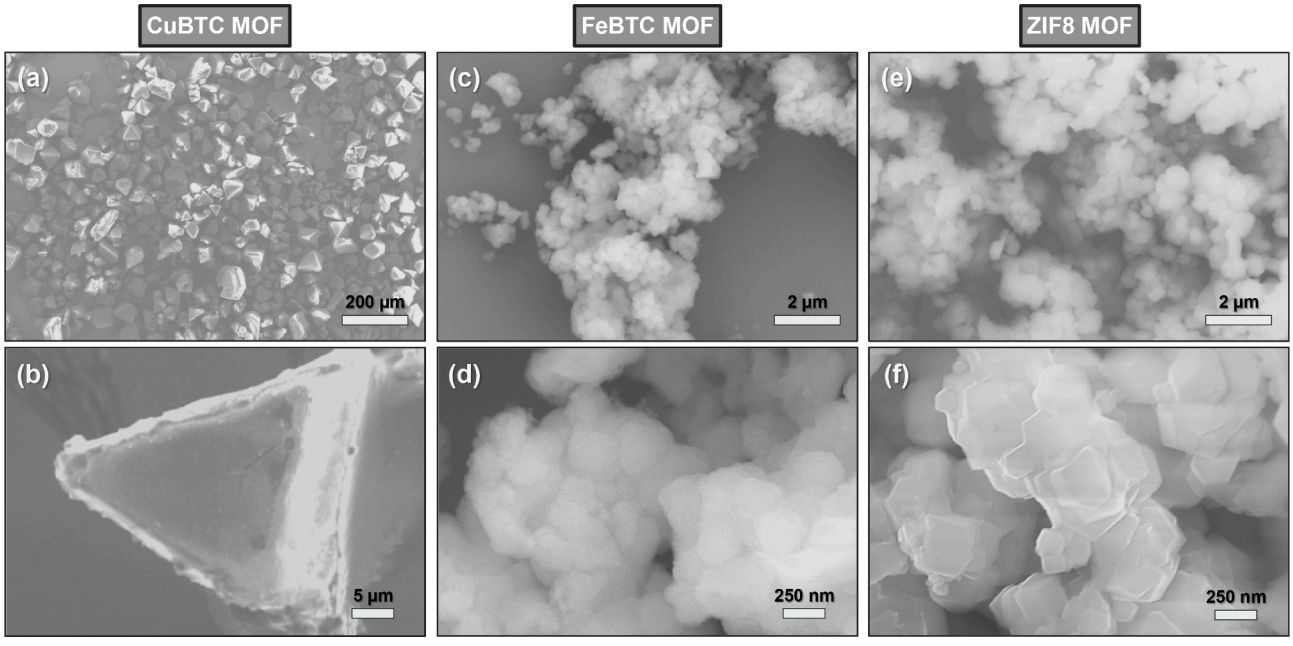

Fig. 2. FE-SEM images of (a-b) CuBTC, (c-d) FeBTC, and (e-f) ZIF8 MOF powders, drop-casted on silicon wafer.

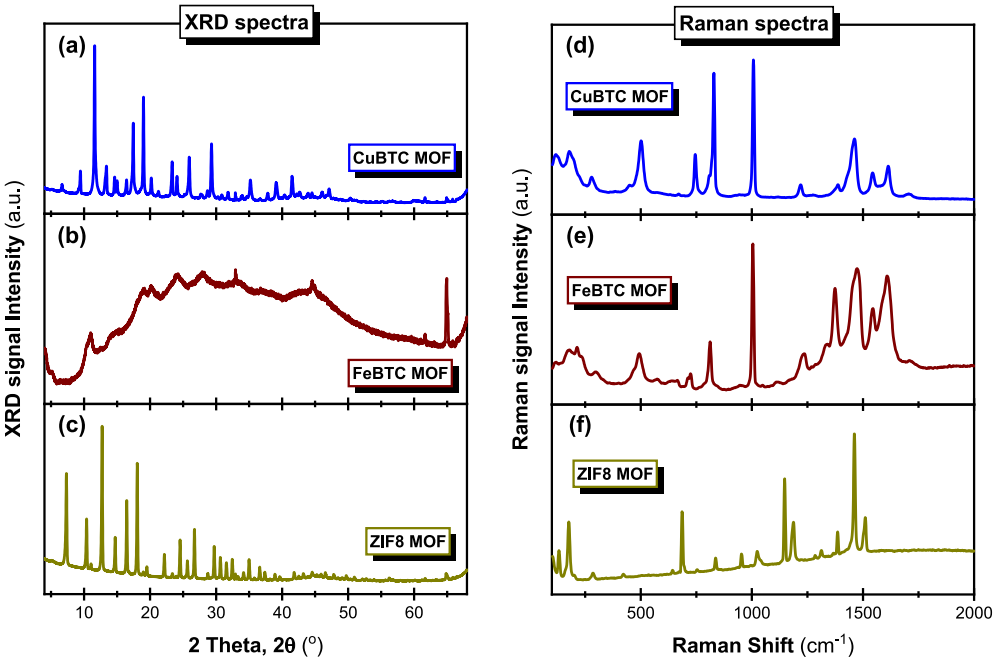

Fig. 3. Left: XRD patterns of (a) CuBTC, (b) FeBTC, and (c) ZIF8 MOF powders. Right: Raman spectra of (d) CuBTC, (e) FeBTC, and (f) ZIF8 MOF powders.

FeBTC, consistent with the literature reports [32–35]. The broad peak shapes with the noisy pattern result from the semi-amorphous nature of FeBTC with micro-crystallite particle size. The XRD pattern of ZIF8 revealed a typical zeolite pattern [36–39] with a rhombic dodecahedral structure, consistent with ICDD #00–062-1030 crystallographic file. Notably, similar to the CuBTC, the ZIF8 also exhibited sharp and well-defined XRD peaks revealing high crystalline nature. Fig. 3c exhibited prominent XRD peaks appearing at 2θ of 7.4°, 10.4°, 12.8°, 14.6°, 16.4°, 18.1°, 22.2°, 24.4°, and 26.7°, which correspond to the (011), (002), (112), (022), (013), (222), (114) (233) and (134) crystal planes of ZIF8, respectively [36,39,40].

The Raman spectroscopic data are illustrated in Fig. 3(d–f) to obtain experimental information about the electronic and vibrational properties of CuBTC, FeBTC and ZIF8 samples, respectively. As per the literature, the Raman spectrum of CuBTC (Fig. 3d) can be distinctly split into two zones, where the first zone in the low-wavenumber range (below 600 cm^{-1}) corresponds to the presence of metal–metal dimer interaction and metal coordination with the organic linker, while the higher-wavenumber zone validates the vibrations of the benzene-1,3,5-tricarboxylate (BTC) ligand [29,41,42]. The Raman band located between 150 to 230 cm^{-1} is associated with the Cu–Cu dimer stretching mode. The vibration modes of Cu–O (related to the oxygen from water adsorbed on Cu^{2+} ions) are observed at 278 cm^{-1}, while a minor peak at 495 cm^{-1} represents the stretching modes of Cu–O related to the oxygen of the carboxylate bridges. In the higher-wavenumber zone, the bands around 744 and 824 cm^{-1} are observed corresponding to the stretching and bending vibrations of the out-of-plane (C–H) ring, respectively. The peaks observed around 1008 and 1611 cm^{-1} correspond to the C = C symmetric stretching modes of the aromatic (benzene) rings of the BTC ligands. Raman peaks located around 1547 cm^{-1} relate to the asymmetric stretching vibration of O–C–O, while that at 1455 cm^{-1} to the symmetric stretching of O–C–O. Similar to the CuBTC, the Raman spectra of FeBTC (Fig. 3e) also exhibit in two zones, as reported earlier [32,34,43]. The first zone below 600 cm^{-1} is associated with the vibrational characteristics of the O-Fe coordination and a Fe-Fe dimer interaction of the exposed metal site. Also, another band can be observed between 620 and 670 cm^{-1}, corresponding to magnetite phase. In the second zone (above 600 cm^{-1}), corresponding to the vibrational modes of the BTC ligand, the major bands were observed at 720 cm^{-1} (stretching vibrations of C–H out-of-plane ring), 816 cm^{-1} (bending modes of C–H out-of-plane ring), 1002 cm^{-1} (C = C stretching modes of benzene rings), 1460 cm^{-1} (symmetrical stretching of O–C–O), 1545 cm^{-1} (asymmetric stretching of O–C–O) and 1609 cm^{-1} (aromatic C = C stretching modes). As observed in Fig. 3f, the ZIF8 exhibited the major Raman peak at 178 cm^{-1} belonging to Zn–N, [38,44] followed by a smaller signal around 282 cm^{-1} assigned to Zn − N stretching [45]. The rest of the wavenumber range (600 to 2000 cm^{-1}) was dominated by intense Raman bands associated with the organic groups of MOF structure. The major bands were observed at 687 cm^{-1} (imidazolium ring puckering), 1025 cm^{-1} (C–H out of plane bend), 1146 cm^{-1} (C5 − N stretching), 1187 cm^{-1} (C–N), 1460 cm^{-1} (C–H bending of methyl), and 1509 cm^{-1} (C4 = C5) [38,44–46].

Fig. 4 displays the high-resolution XPS spectra of the major elements for all three MOF samples identifying the surface chemical composition and phase formation. The elemental survey by XPS, presented in Fig. S8a (Section 4, *Supporting Information*), showed the major contribution from Cu, C and O elements in the CuBTC framework. The C, O, and Cu atomic percentages in CuBTC were 48.55, 42.22, and 9.23 at%, respectively. Significantly high content (atomic%) of C and O elements is consistent with the EDX data revealing the contribution from the high content of graphitic structures in the MOF structure. As observed from XPS survey, FeBTC (Fig. S8b) and ZIF8 (Fig. S8c) exhibit the same trend. Fig. 4(a–c) represents the high-resolution core-level XPS spectra of Cu 2p, C 1 s and O 1 s, collected from the CuBTC sample. As shown in Fig. 4a, the Cu 2p core-level spectrum is composed of two spin–orbit double peaks, ascribed to Cu $2p^{3/2}$ (936.2 eV) and Cu $2p^{1/2}$ (956.3 eV), with two satellite peaks confirming the presence of Cu^{2+} oxidation state [28,47–49]. Further deconvolution revealed the presence of both the oxidation states, namely Cu^{2+} in cupric oxide and Cu^{+} in cuprous oxide. The Cu $2p^{3/2}$ components for Cu^{2+} appear around 936.1 and 940.6 eV, while the corresponding Cu $2p^{1/2}$ components are around 955.4 and 963.1 eV. Similarly, the Cu^{+} exhibited its $2p^{3/2}$ peak at 934.5 eV and Cu $2p^{1/2}$ peaks around 944.7 and 953.1 eV. The core-level C 1 s spectrum (Fig. 4b) could be deconvoluted into four well-fitted components, sp^2 carbons (≈284.5 eV), sp^3 carbons (≈285 eV), C–O (≈286 eV), –O–C = O (≈288.6 eV) groups of the BTC linker; and a satellite for π–π* bonds (~289.9 eV) originated from the benzene ring in the ligand. The O 1 s spectrum (Fig. 4c) exhibited three peaks originating from the Cu–O bond

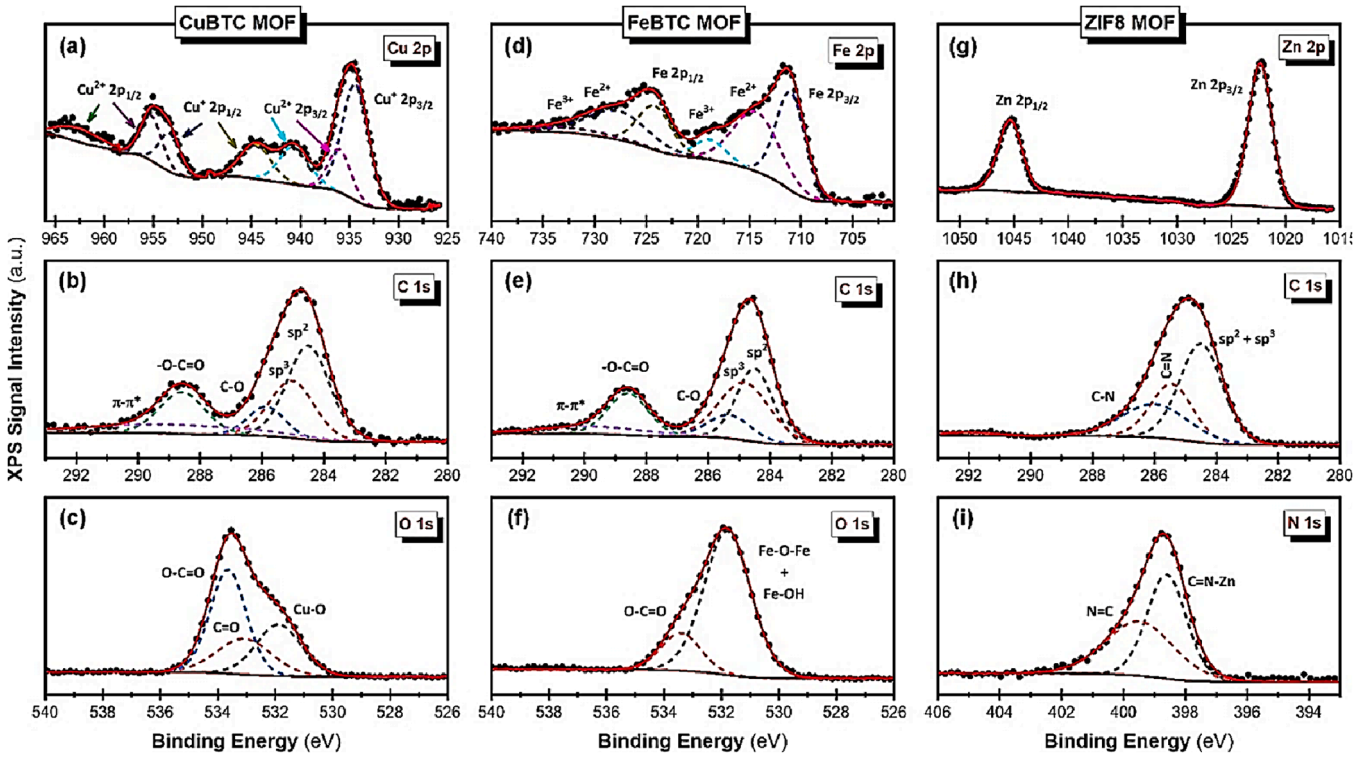

Fig. 4. Core-level XPS spectra of (a-c) CuBTC MOF [(a) Cu 2p, (b) C 1 s, (c) O 1 s]]; (d-f) FeBTC MOF [(d) Fe 2p, (e) C 1 s, (f) O 1 s]], and (g-i) ZIF8 MOF [(g) Zn 2p, (h) C 1 s, (i) N 1 s]].

(531.8 eV) and C = O bond (533.1 eV) peaks, apart from the –O–C = O (533.6 eV) component.

From the survey scan, the FeBTC MOF was found to consist of Fe, C and O elements, as observed in Fig. S8b [50,51]. The C, O, and Fe atomic percentages in FeBTC are 58.46, 29.74, and 11.81 at%, respectively. The high-resolution Fe 2p XPS spectrum displayed two peaks at 710.98 eV and 724.36 eV, attributed to Fe $2p^{3/2}$ and Fe $2p^{1/2}$ (Fig. 4d). Further deconvolution provides two satellite bands attributed to Fe^{2+} located at 714.6 and 728 eV and two others corresponding to Fe^{3+} around 718.8, and 731.8 eV, indicating both Fe^{2+} and Fe^{3+} ions coordinated with BTC.

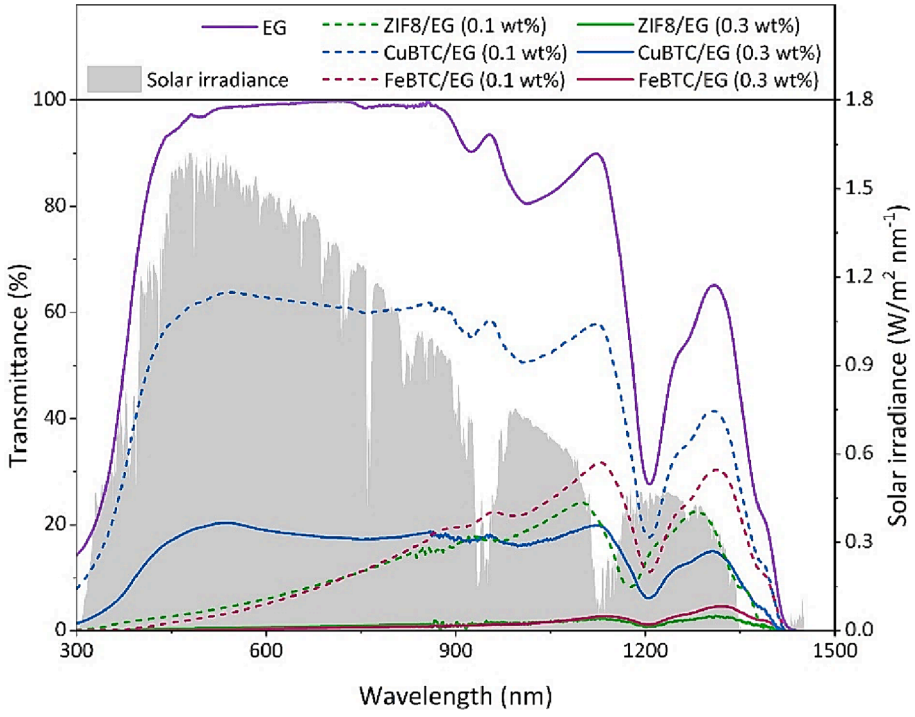

Fig. 5. Transmittance of the base fluid EG, and CuBTC/EG, ZIF8/EG and FeBTC/EG dispersions at two different concentrations, as well as the spectral solar irradiance in the background.

The C 1 s spectrum (Fig. 4e) revealed the presence of five components, with the first two related sp^2 and sp^3 carbons (≈284.5 and 285 eV, respectively), followed by C–O (≈285.7 eV) and –O–C = O (≈288.6 eV) groups of the BTC linker, and π–π* bonds around 290 eV. The O 1 s spectrum exhibited the major contribution from the Fe–O–Fe and Fe–OH observed at 531.8 eV, apart from the –O–C = O (533.4 eV) component (Fig. 4f). For the ZIF8 framework, the elemental survey, shown in Fig. S8c, indicated the major contribution from Zn, C, O, and N elements [40,52]. The C, N, O, and Zn atomic percentages in ZIF8 are 56.94, 20.75, 7.58, and 14.73 at%, respectively. Fig. 4g shows the high-resolution XPS spectrum of Zn 2p, displaying divalent Zn $2p^{3/2}$ and Zn $2p^{1/2}$ peaks at a binding energy of ≈1022 eV and ≈1045 eV. The C 1 s spectrum (Fig. 4h) revealed the contribution of the sp^2 carbons (≈284.5 eV) with two other peaks associated with C = N (285.5 eV) and C–N bonds (286.05 eV) on the imidazole ring. The N 1 s XPS spectrum (Fig. 4i) is mainly contributed by the peak at 398.6 eV related to C = N–Zn and that at 399.5 eV corresponds to N = C. Notably, for ZIF8 MOF powders, the N element becomes the second highest next to C, overshadowing the O contribution in MOF formation. In contrast, in the BTC-based MOFs, CuBTC and FeBTC, the O plays a crucial role in framework formation, having almost similar content (atomic%) to C.

3.2. Optical properties of MOF dispersion based fluids

Fig. 5 shows the transmittance measured for the three MOF/EG dispersions at two mass fractions of 0.1 and 0.3 wt% across a wavelengths range of 300–1500 nm. It also depicts the spectral solar irradiation to indicate the variation of intensity distribution with respect to the transmittance patterns of the MOF/EG. It could be seen that the base fluid EG absorbed well in the near infrared region and nearly transparent at lower wavelengths, where MOF/EG dispersions are sought to prevent such a high loss. For instance, from 80 % to 100 % of the light was unabsorbed by EG within the region between 400 nm and 1150 nm, which makes more than three quarters of the total solar energy across the full range which is ~ 1000 W/m^2. This loss in radiation through EG decreased sharply by adding MOF powders to drop below 20 % for all MOF/EG dispersions except for CuBTC/EG at 0.1 wt% across the entire range as well as FeBTC/EG at 0.1 wt% in narrow regions at wavelengths above 900 nm, where solar radiation is relatively low, while FeBTC/EG and ZIF8/EG at the higher mass fraction of 0.3 wt% exhibited nearly zero transmittance across most of the full range.

Low transmittance, however, cannot be translated directly into high absorption without taking scattering into account since light may be scattered by the dispersed particles as it travels through the fluid, and lost if not re-absorbed after multiple scattering by neighbouring particles. Therefore, we also measured scattering using an integrating sphere and then both transmittance and scattering measurements were used to calculate the absorption (μ_a, Equation S13) and scattering coefficients (μ_s, Equation S14, see *Supporting Information*, Section 2, for calculation procedures). Fig. 6 depicts both absorption and scattering coefficients over the wavelength range of interest of 400–900 nm, where the base fluid is almost fully transparent (Fig. 5). This fact that low transmittance cannot be generally translated into high absorption is evident in the case of the ZIF8/EG, which exhibited nearly zero absorption (Fig. 6a) with all light scattered (Fig. 6b) and lost as detected by the integrating sphere system as transmitted light (Fig. 5). The scattering coefficient at the lower mass concentration of ZIF8 (0.1 wt%) decreased linearly from 4 to 2 cm^{-1} with the increase in wavelength within the range of interest. By increasing the mass concentration of ZIF8 to 0.3 wt%, the ZIF8/EG exhibited a higher scattering coefficient of a similar pattern but with a lower decreasing rate (from 5.5 to 4.5 cm^{-1}) with the increase in wavelength (from 400 to 900 nm). Such high scattering with zero absorption is enough to declare that ZIF8 MOF is not the appropriate candidate for solar absorption-based applications.

On the other hand, CuBTC/EG and FeBTC/EG exhibited different patterns of absorption and scattering over the wavelength range of interest. In detail, CuBTC/EG showed ability to absorb across the full range of interest with exception for wavelengths below 600 nm where the absorption coefficient decreased gradually to reach zero value at 500 nm and back to increase at lower wavelength, where the solar energy content could be negligible. Thus, we may say that the CuBTC/EG at mass concentrations of 0.3 wt% absorbed well at wavelength higher than 600 nm with an approximately constant absorption coefficient of 1.25 ± 0.1 cm^{-1}, while the lower concentration of the same sample (0.1 wt%) showed the same pattern but with a much lower absorption coefficient of 0.3 ± 0.08 cm^{-1}. This weakness in absorption of both CuBTC/EG at wavelengths below 600 nm is attributed to the loss in radiation by scattering in this region as can be seen in Fig. 6b. In contrast, FeBTC/EG exhibited high absorption at wavelengths below 600 nm, with most of the light was scattered at higher wavelengths within the range of interest (400–900 nm). The absorption coefficient of FeBTC dispersed at 0.3 wt% in EG reached as high as 8 cm^{-1} at 400 nm

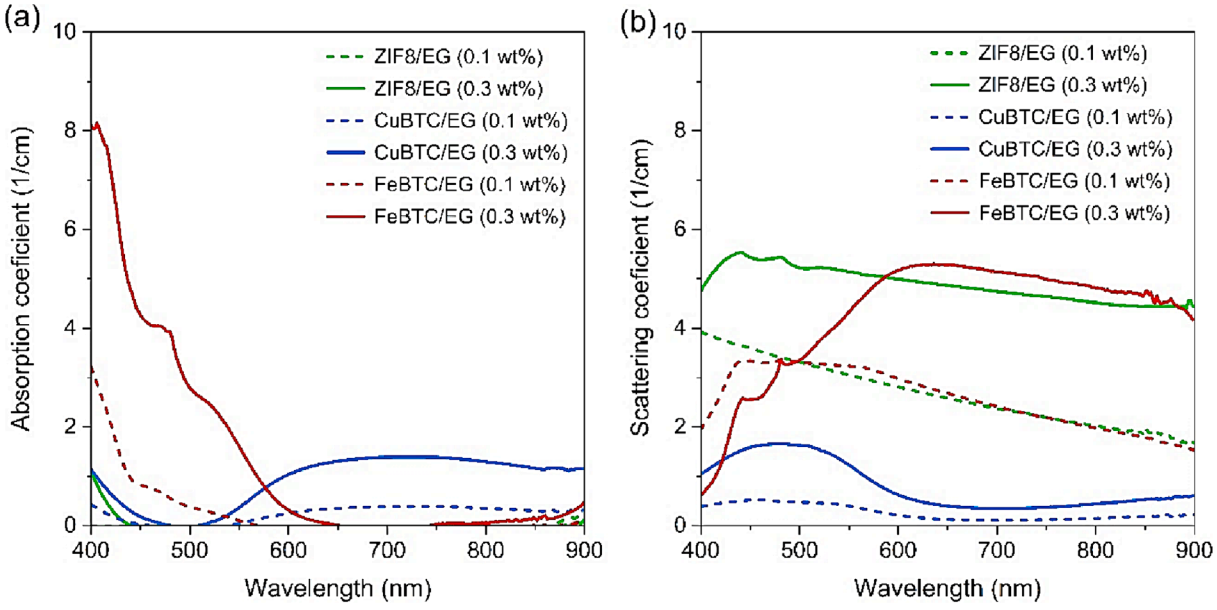

Fig. 6. (a) Absorption and (b) scattering coefficients of ZIF8/EG, CuBTC/EG and FeBTC/EG at two mass concentrations of 0.1 and 0.3 wt%.

which sharply decreased in a an approximately linear relationship to zero at 660 nm (i.e., a decrease rate of 0.0.12 cm^{-1}/nm). By decreasing the concentration of FeBTC to 0.1 wt%, the absorption coefficient showed the same pattern but at lower values. These results reveal that, despite that the three types of these MOF dispersion based fluids being quite effective at light scattering over different wavelength regions, two of them exhibited high levels of absorption, particularly the FeBTC at 0.3 wt%, which represents our optimal solar absorber in this work.

3.3. STEC characteristics of MOF dispersion based fluids

The combined effect of both solar absorption and thermal transport within the MOF particles, the base fluid EG, and the MOF-EG interface was evaluated by the variation in temperature of the MOF/EG under light exposure, as plotted in Fig. 7. From the onset of solar exposure, pure EG showed a moderate temperature rise, reaching approximately 31 °C after half an hour. This increment was slightly amplified in the ZIF8/EG, with the 0.1 and 0.3 wt% concentrations peaking at around 31.7 °C and 33 °C respectively. In contrast, the CuBTC/EG exhibited more pronounced thermal response, with temperatures ascending to 37.6 °C at 0.1 wt% and 39.5 °C at 0.3 wt%. The FeBTC/EG demonstrated the most substantial temperature enhancement, achieving the highest recorded temperatures of 38.4 °C and 43 °C for 0.1 and 0.3 wt% concentrations respectively. However, it is crucial to recognize that these temperature profiles alone do not provide a complete evaluation of the performance of MOF/EG. The container (petri dish, shown in Fig. 1b) lacked thermal insulation, which may have led to a disparity between the observed temperature increase and the actual STEC efficiency. Heat loss through the container walls could result in a slower rise in temperature and limit the potential increase, especially over extended periods of irradiation. To address this limitation and provide a more accurate assessment of the STEC efficiency, we have adjusted our evaluation to account for heat losses. This adjustment ensures that the efficiency calculated reflects the true performance of the MOF dispersion based fluid in converting solar energy to thermal energy. The corrected analysis offers a more realistic perspective on how each MOF/EG would perform in a practical setting, where thermal insulation and heat retention were optimized.

Fig. 8 provides a comparative analysis of STEC efficiency (estimated by Equation (1) and the specific absorption rate (SAR, calculated by Equation (4) for MOF/EG at different mass concentrations. Fig. 8a showcased the STEC efficiency for pure EG as well as ZIF8/EG, CuBTC/EG, and FeBTC/EG at 0.1 and 0.3 wt% mass concentrations. Pure EG alone exhibited a modest STEC efficiency of 15 %, attributed to its inherent absorption properties in the ultraviolet (UV) and near-infrared (NIR) spectra. The inclusion of ZIF8 into the EG at the studied concentrations yielded a negligible improvement in STEC efficiency, increasing by only 1 % and 4 % respectively, which correlates with the previously discussed optical characteristics of near-zero absorption and high scattering. In contrast, the introduction of CuBTC and FeBTC to EG significantly enhances the STEC efficiency. The concentration of 0.1 wt%, CuBTC/EG and FeBTC/EG improved STEC efficiency to 30 % and 31 %, respectively. An increase in concentration to 0.3 wt% led to further enhancement, with CuBTC/EG reaching STEC efficiency of 33.5 % and FeBTC/EG achieving the highest efficiency of 41 %, making it the most effective MOF dispersion based fluid in this study for solar thermal applications. Fig. 8b illustrates the SAR values, indicating the thermal energy generation capacity per unit mass of the MOF particles upon light absorption. The data revealed an inverse relationship between MOF concentration and SAR for all three MOF/EG disersions. Specifically, FeBTC exhibited a SAR of 34 kW/gnp at a lower concentration of 0.1 wt %, which markedly decreased to 18.3 kW/gnp at the increased concentration of 0.3 wt%. This demonstrates that while higher MOF concentrations can enhance STEC efficiency, they do so at the cost of reduced SAR, implying a diminishing return on energy generation capacity per additional unit of mass. The observed inverse trend suggests a complex interaction between MOF concentration and light absorption efficiency. At lower concentrations, the MOF particles are more dispersed, potentially allowing for greater interaction with light and more effective heat conversion per particle. As the concentration increases, particle–particle interactions may lead to a reduced surface area available for light absorption per unit mass, thus lowering the SAR [53,54]. This outcome necessitates a careful consideration of the balance between achieving high STEC efficiency and maintaining a cost-effective SAR, especially when scaling up for practical applications. Optimizing this balance is crucial for the development of economically viable solar thermal systems. It requires a detailed understanding of the interplay between dispersed particle loading, light absorption, and thermal energy conversion. These insights are vital for designing fluid-based solar collectors that can efficiently harness solar energy while remaining financially sustainable. The findings also highlight the need for further research into the mechanisms of light interaction with densely packed particles and the development of strategies to maximize the SAR without compromising STEC efficiency.

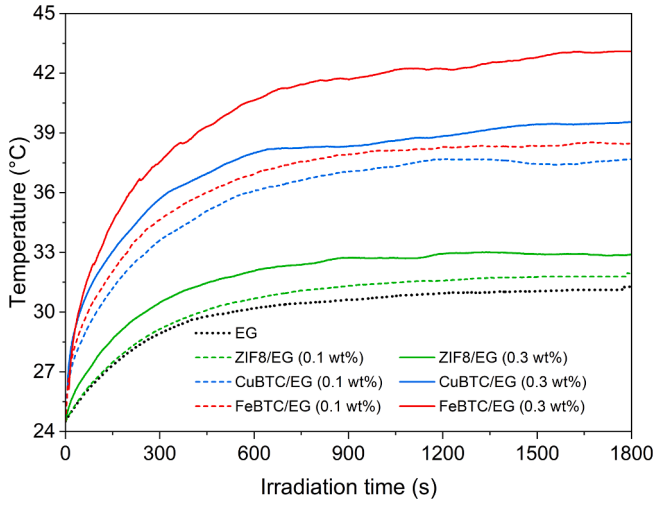

Fig. 7. (a) Temperature variation of ZIF8/EG, CuBTC/EG and FeBTC/EG at two mass concentrations of 0.1 and 0.3 wt%.

3.4. Dispersion stability of MOF/EG over time

To ensure the viability of MOF dispersion for real-world applications, a rigorous examination of their dispersion stability over time is essential, as this directly impacts their optical properties and, consequently, their performance in STEC systems. In our detailed investigation, we focused on FeBTC/EG, identified as the prime MOF dispersion based fluid due to its superior absorption and STEC performance relative to others at an identical concentration of 0.3 wt%. The change in transmittance and scattering were measured over a period of 60 days (D0, D5, D15, D30 and D60, where D denotes day) as well as after shaking in the D60 (see Fig. 9a for the transmittance). The results indicated that within the initial five days, transmittance alterations were minimal, with only a slight increase in the wavelengths extending above 800 nm. By Day 15, a slight yet discernible elevation in transmittance was observed, remaining under 8 % for wavelengths below 700 nm, then increased at a higher rate to 22 % at 900 nm. At a longer period of 30 days, transmittance at wavelengths below 700 nm stayed below 30 % but showed a linear progression to 50 % at 900 nm. At the 60-day mark, the data revealed a significant increase in transmittance, suggesting the FeBTC/EG had reached a level of transparency indicative of complete sedimentation under the influence of gravity. To probe the potential for particle agglomeration—a phenomenon that could negatively affect the functionality FeBTC/EG — the sample underwent manual agitation. After shaking, the transmittance values recorded approximated those

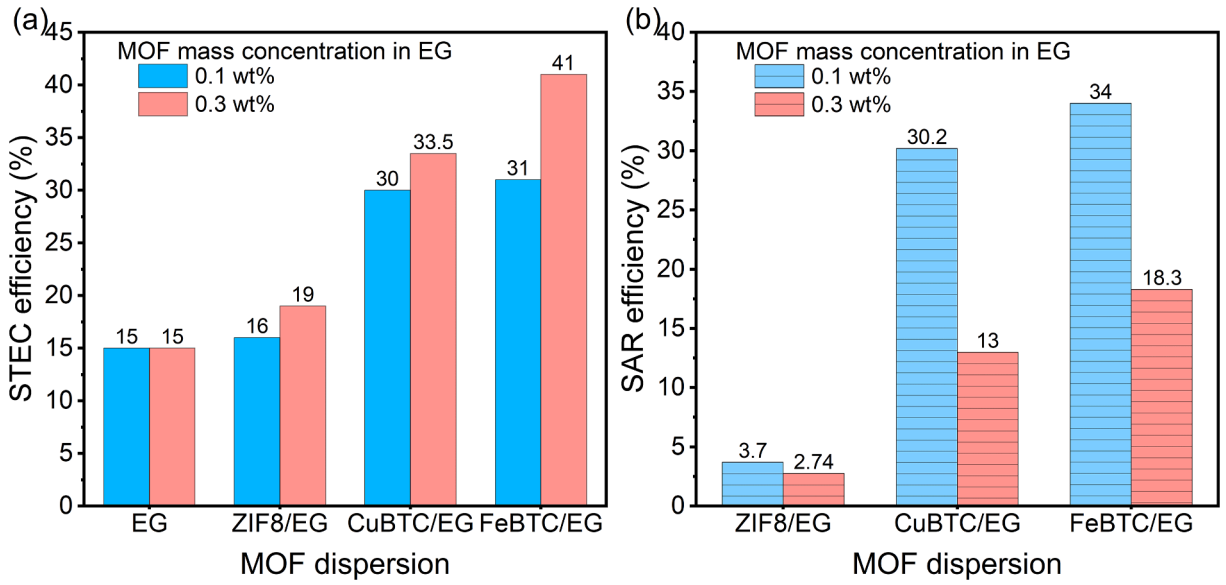

Fig. 8. (a) STEC efficiency and (b) SAR of ZIF8/EG, CuBTC/EG and FeBTC/EG at two mass concentrations of 0.1 and 0.3 wt%.

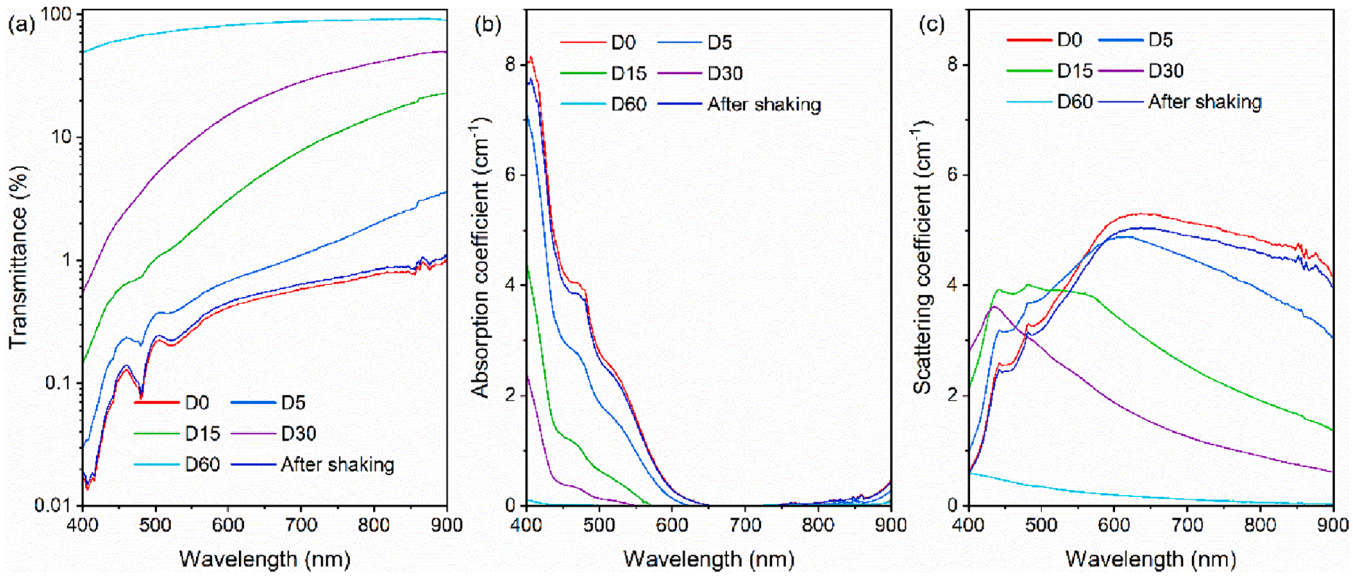

Fig. 9. Monitoring the dispersion stability over 60 days for FeBTC MOF in EG at 0.3 wt% mass concentration: (a) transmittance, (b) absorption coefficient, and (c) scattering coefficient.

observed at the outset of the experiment (Day 0), suggesting reversibility of sedimentation. However, this alone does not confirm the absence of agglomeration effect; a thorough assessment must also consider the behaviour of absorption and scattering separately. Upon review of the absorption and scattering coefficients as depicted in Fig. 9b and c, a gradual decline over the 60-day period was noted, yet these parameters nearly reverted to their initial values following the shaking procedure. This pattern suggests that the decrease in both absorption and scattering was attributable primarily to sedimentation (under the effect of gravity) rather than agglomeration. Notably, for dynamic systems where MOF dispersion is in continuous circulation, the concern for sedimentation is mitigated as the constant movement prevents the settling of the dispersed particles. Our study highlights the importance of considering the dynamic nature of practical systems when evaluating the MOF dispersion based fluids. In such environments, the effects of sedimentation are naturally counteracted by fluid movement, ensuring consistent distribution and suspension of MOF particles. These findings are significant as they not only demonstrate the high performance of FeBTC/EG in terms of optical properties and STEC efficiency but also affirm its suitability for dynamic applications where sedimentation could otherwise be a concern. The ability to maintain dispersion stability over time is crucial for the long-term operational stability and efficiency of solar thermal systems employing MOF dispersion based fluids.

4. Conclusion

This work presents a study on the optical properties and STEC characteristics of three types of MOF/EG dispersions. Specifically, the MOFs studied were CuBTC, FeBTC, and ZIF8, with mass fractions of 0.1 and 0.3 wt%. The optical properties of the dispersions revealed that the base fluid, EG, absorbed well in the near infrared region but was nearly transparent at lower wavelengths, with up to 100 % of light unabsorbed between 400 nm and 1150 nm. Upon dispersing MOF in EG, the loss in

radiation through EG decreased sharply, dropping below 20 %, except for CuBTC/EG at 0.1 wt% and FeBTC/EG at 0.1 wt% in certain wavelength regions. The dispersion with ZIF8 demonstrated almost zero absorption with all light scattered, rendering it inappropriate for use in solar absorption-based applications. On the contrary, CuBTC/EG and FeBTC/EG demonstrated significant absorption over the wavelength range of interest. In particular, the FeBTC MOF dispersed at 0.3 wt% in EG reached an absorption coefficient as high as 8 cm^{-1} at 400 nm, decreasing linearly to zero at 660 nm, making it an optimal solar absorber in this study. The STEC characteristics were evaluated by measuring the temperature change of the MOF/EG under light exposure. The FeBTC/EG, with a concentration of 0.3 wt%, achieved the highest temperature of 43 °C after 30 min of irradiation and the highest STEC efficiency of 41 %, marking it as the optimal MOF dispersion based fluid in this study. The dispersion stability of MOF/EG was also evaluated, with the focus on FeBTC/EG. There was a negligible change in transmittance during the first five days, with a modest rise at wavelengths above 800 nm. The transmittance increased very slightly after 15 days but reached higher values after 60 days, which was enough to render the MOF dispersion almost transparent due to full sedimentation under gravity. However, there was no agglomeration observed in the sample, and the reduction in the absorption and scattering was only due to sedimentation under the effect of gravity. Overall, the study reveals promising prospects of using MOF dispersion based fluid, particularly FeBTC/EG, for solar absorption-based applications. However, balancing the trade-off between the cost and STEC efficiency when adding more MOF particles, and managing the impact of sedimentation on the optical properties in static conditions, will be key challenges to address for their practical application. Considering the costs of MOFs (FeBTC-£16.5/g, ZIF8-£49/g, and CuBTC-£25/g; sourced from Sigma-Aldrich) and STEC efficiencies of these three MOF/EG dispersions; FeBTC emerges as the optimal choice of MOF materials, blending efficiency with economic viability. FeBTC/EG not only demonstrates high STEC efficiency but also offers a cost-effective solution, highlighting the importance of cost-efficiency balance in selecting MOF materials for solar absorption applications. However, the estimation of true cost is difficult at this stage and may provide inaccurate values as the cost depends on several factors such as the sourcing procedure of the chemicals as the cost varies significantly depending on the sourcing company or inhouse production, the solar thermal liquid preparation process, the design of the solar thermal collector and many more. Future work should aim at optimizing this balance to enhance both economic and operational feasibility.

CRediT authorship contribution statement

Hussein Sayed Moghaieb: Data curation, Investigation, Methodology, Validation, Writing – original draft, Writing – review & editing. **Sameh Khalil:** Data curation, Investigation, Methodology, Validation, Writing – review & editing. **Abhijit Ganguly:** Validation, Writing – original draft, Writing – review & editing, Data curation, Investigation, Methodology. **Paul Maguire:** Funding acquisition. **Davide Mariotti:** Funding acquisition, Project administration, Resources. **Supriya Chakrabarti:** Conceptualization, Funding acquisition, Investigation, Methodology, Supervision, Validation, Visualization, Writing – original draft, Writing – review & editing, Project administration, Resources.

Declaration of Competing Interest

The authors declare that they have no known competing financial interests or personal relationships that could have appeared to influence the work reported in this paper.

Acknowledgement

S.C. thanks the support of the Department for the Economy (DfE), Northern Ireland, under the US-Ireland R&D Partnership Programme, reference number: USI160.

Appendix A. Supplementary data

Experimental details (chemicals, fluids); principle and equations used to calculate the optical and STEC; Figures for the supporting studies.

The following files are available free of charge.

Supplementary data to this article can be found online at https://doi.org/10.1016/j.solener.2024.112542.

References

[1] R. Adib, H.E. Murdock, F. Appavou, A. Brown, B. Epp, A. Leidreiter, et al., Renewables 2015 global status report, REN21 Secr Paris, Fr, 2015, p. 162.
[2] Sieminski A. International energy outlook 2013. US Energy Inf Adm Rep Number DOE/EIA-0484. 2013.
[3] N.S. Lewis, Introduction: Solar Energy Conversion, Chem Rev [internet]. 115 (23) (2015 Dec 9) 12631–12632, https://doi.org/10.1021/acs.chemrev.5b00654. Available from:.
[4] V.H. Dalvi, S.V. Panse, J.B. Joshi, Solar thermal technologies as a bridge from fossil fuels to renewables, Nat Clim Chang [internet]. 5 (11) (2015) 1007–1013, https://doi.org/10.1038/nclimate2717. Available from:.
[5] A. Lenert, E.N. Wang, Optimization of nanofluid volumetric receivers for solar thermal energy conversion, Available from: Sol Energy [internet]. 86 (1) (2012) 253–265 https://www.sciencedirect.com/science/article/pii/S0038092X11003550 https://doi.org/10.1016/j.solener.2011.09.029.
[6] Chamsa-ard W, Brundavanam S, Fung CC, Fawcett D, Poinern G. Nanofluid types, their synthesis, properties and incorporation in direct solar thermal collectors: A review. Vol. 7, Nanomaterials. 2017. DOI:10.3390/nano7060131.
[7] J.E. Minardi, H.N. Chuang, Performance of a "black" liquid flat-plate solar collector, Sol. Energy 17 (3) (1975) 179–183.
[8] T.P. Otanicar, P.E. Phelan, J.S. Golden, Optical properties of liquids for direct absorption solar thermal energy systems, Sol Energy [internet]. 83 (7) (2009) 969–977, https://doi.org/10.1016/j.solener.2008.12.009. Available from:.
[9] Amjad M, Jin H, Du X, Wen D. Experimental photothermal performance of nanofluids under concentrated solar flux. Sol Energy Mater Sol Cells [Internet]. 2018;182:255–62. Available from: https://www.sciencedirect.com/science/article/pii/S0927024818301569 DOI:https://doi.org/10.1016/j.solmat.2018.03.044.
[10] A.S. Abdelrazik, M.A.M. Sayed, H. Hashim, A.M.A. Omar, M.H.M. Helmy, A. Oulguidoum, et al., A guide to the preparation techniques of six classes of metal-, metal oxide-, and carbon-based nanofluids and the implications for their stability, J. Therm. Anal. Calorim. 148 (17) (2023) 8793–8839.
[11] S. Kumar, N. Chander, V.K. Gupta, R. Kukreja, Progress, challenges and future prospects of plasmonic nanofluid based direct absorption solar collectors – A state-of-the-art review, Sol. Energy 227 (2021) 365–425.
[12] S. Sreekumar, A. Ganguly, S. Khalil, S. Chakrabarti, N. Hewitt, J.D. Mondol, et al., Thermo-optical characterization of novel MXene/Carbon-dot hybrid nanofluid for heat transfer applications, . Available from: J Clean Prod [internet]. 434 (2024) 140395 https://www.sciencedirect.com/science/article/pii/S0959652623045535 https://doi.org/10.1016/j.jclepro.2023.140395.
[13] D. Wang, L. Wang, G. Zhu, W. Yu, J. Zeng, X. Yu, et al., Magnetic photothermal nanofluids with excellent reusability for direct absorption solar collectors, ACS Appl Energy Mater. 1 (8) (2018) 3860–3868.
[14] V.-D. Dao, N.H. Vu, S. Yun, Recent advances and challenges for solar-driven water evaporation system toward applications, . Available from: Nano Energy [internet]. 68 (2020) 104324 https://www.sciencedirect.com/science/article/pii/S2211285519310316 https://doi.org/10.1016/j.nanoen.2019.104324.
[15] M. Gao, L. Zhu, C.K. Peh, G.W. Ho, Solar absorber material and system designs for photothermal water vaporization towards clean water and energy production, Energy Environ Sci [internet]. 12 (3) (2019) 841–864, https://doi.org/10.1039/C8EE01146J. Available from:.
[16] G. Liu, J. Xu, K. Wang, Solar water evaporation by black photothermal sheets, Available from: Nano Energy [internet]. 41 (2017) 269–284 https://www.sciencedirect.com/science/article/pii/S2211285517305451 https://doi.org/10.1016/j.nanoen.2017.09.005.
[17] H. Wu, C. Liu, Z. Zhu, Y. Shao, J. Lin, J. Wen, et al., Nanoporous Silicon Dioxide Films for Large Area and Low-Cost Fabrication of Ultra-Low Refractive Index Coatings, ACS Appl Nano Mater. 6 (17) (2023) 15437–15444.
[18] C. Wu, H. Geng, S. Tan, J. Lv, H. Wang, Z. He, et al., Highly efficient solar anti-icing/deicing via a hierarchical structured surface, Mater Horizons. 7 (8) (2020) 2097–2104.
[19] Y. Xia, X. Pu, J. Liu, J. Liang, P. Liu, X. Li, et al., CuO nanoleaves enhance the c-Si solar cell efficiency, J Mater Chem A [internet]. 2 (19) (2014) 6796–6800, https://doi.org/10.1039/C4TA00097H. Available from:.
[20] Y. Wang, C. Wang, X. Song, M. Huang, S.K. Megarajan, S.F. Shaukat, et al., Improved light-harvesting and thermal management for efficient solar-driven water evaporation using 3D photothermal cones, J Mater Chem A [internet]. 6 (21) (2018) 9874–9881, https://doi.org/10.1039/C8TA01469H. Available from:.
[21] H. Ren, M. Tang, B. Guan, K. Wang, J. Yang, F. Wang, H.G. Foam, for Efficient Omnidirectional Solar-Thermal Energy Conversion. Adv Mater [Internet]., et al., 1;

29(38):1702590, Available from: (2017 Oct), https://doi.org/10.1002/adma.201702590.
[22] H.K. Raut, V.A. Ganesh, A.S. Nair, S. Ramakrishna, Anti-reflective coatings: A critical, in-depth review, Energy Environ Sci [internet]. 4 (10) (2011) 3779–3804, https://doi.org/10.1039/C1EE01297E. Available from:.
[23] A.F. Payam, S. Khalil, S. Chakrabarti, Synthesis and characterization of MOF derived structures: recent advances and future perspectives, Small (2024), https://doi.org/10.1002/smll.202310348.
[24] Moghaieb HS, Amendola V, Khalil S, Chakrabarti S, Maguire P, Mariotti D. Nanofluids for Direct-Absorption Solar Collectors—DASCs: A Review on Recent Progress and Future Perspectives. Vol. 13, Nanomaterials. 2023. DOI: 10.3390/nano13071232.
[25] H.S. Moghaieb, D.B. Padmanaban, P. Kumar, A.U. Haq, C. Maddi, R. McGlynn, et al., Efficient solar-thermal energy conversion with surfactant-free Cu-oxide nanofluids, . Available from: Nano Energy [internet]. 108 (2023) 108112 https://www.sciencedirect.com/science/article/pii/S2211285522011909 https://doi.org/10.1016/j.nanoen.2022.108112.
[26] S.J. Madsen, B.C. Wilson, Optical properties of brain tissue, Opt Methods Instrum Brain Imaging Ther. (2012) 1–22.
[27] H. Zhang, H.-J. Chen, X. Du, D. Wen, Photothermal conversion characteristics of gold nanoparticle dispersions, Available from: Sol Energy [internet]. 100 (2014) 141–147 https://www.sciencedirect.com/science/article/pii/S0038092X13005215 https://doi.org/10.1016/j.solener.2013.12.004.
[28] Bodkhe GA, Hedau BS, Deshmukh MA, Patil HK, Shirsat SM, Phase DM, et al. Detection of Pb(II): Au Nanoparticle Incorporated CuBTC MOFs [Internet]. Vol. 8, Frontiers in Chemistry . 2020. Available from: https://www.frontiersin.org/article/10.3389/fchem.2020.00803.
[29] R. Nivetha, A. Sajeev, A. Mary Paul, K. Gothandapani, S. Gnanasekar, P. Bhardwaj, et al., Cu based Metal Organic Framework (Cu-MOF) for electrocatalytic hydrogen evolution reaction, Mater Res Express [internet]. 7 (11) (2020) 114001, https://doi.org/10.1088/2053-1591/abb056. Available from:.
[30] L. Zhi, H. Liu, Y. Xu, D. Hu, X. Yao, J. Liu, Pyrolysis of metal–organic framework (CuBTC) decorated filter paper as a low-cost and highly active catalyst for the reduction of 4-nitrophenol, Dalt Trans [internet]. 47 (43) (2018) 15458–15464, https://doi.org/10.1039/C8DT03327G. Available from:.
[31] Fu D, Li H, Zhang X-M, Han G, Zhou H, Chang Y. Flexible solid-state supercapacitor fabricated by metal-organic framework/graphene oxide hybrid interconnected with PEDOT. Mater Chem Phys [Internet]. 2016;179:166–73. Available from: https://www.sciencedirect.com/science/article/pii/S0254058416303443 DOI: https://doi.org/10.1016/j.matchemphys.2016.05.024.
[32] Castañeda-Ramírez AA, Rojas-García E, López-Medina R, García-Martínez DC, Nicolás- Antúnez J, Maubert-Franco AM. Magnetite nanoparticles into Fe-BTC MOF as adsorbent material for the remediation of metal (Cu(II), Pb(II, As(III) and Hg(II)) ions-contaminated water. Catal Today [Internet]. 2021; Available from: https://www.sciencedirect.com/science/article/pii/S0920586121004880 DOI:https://doi.org/10.1016/j.cattod.2021.11.007.
[33] Conde-González JE, Peña-Méndez EM, Melián-Fernández AM, Havel J, Salvadó V. Synthesis, performance and mechanism of nanoporous Fe-(1,3,5-tricarboxylic acid) metal-organic framework in the removal of anionic dyes from water. Environ Nanotechnology, Monit Manag [Internet]. 2021;16:100541. Available from: https://www.sciencedirect.com/science/article/pii/S2215153221001161 DOI: https://doi.org/10.1016/j.enmm.2021.100541.
[34] A.A. Castañeda Ramírez, E. Rojas García, R. López Medina, J.L. Contreras Larios, R. Suárez Parra, A.M. Maubert Franco, Selective Adsorption of Aqueous Diclofenac Sodium, Naproxen Sodium, and Ibuprofen Using a Stable Fe3O4–FeBTC Metal-Organic, Framework Vol. 14 (2021) Materials, https://doi.org/10.3390/ma14092293.
[35] Oveisi AR, Khorramabadi-zad A, Daliran S. Iron-based metal–organic framework, Fe(BTC): an effective dual-functional catalyst for oxidative cyclization of bisnaphthols and tandem synthesis of quinazolin-4(3H)-ones. RSC Adv [Internet]. 2016;6(2):1136–42. Available from: https://doi.org/10.1039/C5RA19013D DOI: 10.1039/C5RA19013D.
[36] Luanwuthi S, Krittayavathananon A, Srimuk P, Sawangphruk M. In situ synthesis of permselective zeolitic imidazolate framework-8/graphene oxide composites: rotating disk electrode and Langmuir adsorption isotherm. RSC Adv [Internet]. 2015;5(58):46617–23. Available from: https://doi.org/10.1039/C5RA05950J DOI:10.1039/C5RA05950J.
[37] Bergaoui M, Khalfaoui M, Awadallah-F A, Al-Muhtaseb S. A review of the features and applications of ZIF-8 and its derivatives for separating CO2 and isomers of C3- and C4- hydrocarbons. J Nat Gas Sci Eng [Internet]. 2021;96:104289. Available from: https://www.sciencedirect.com/science/article/pii/S187551002100487X DOI:https://doi.org/10.1016/j.jngse.2021.104289.
[38] Xu B, Xu W, Wang G, Liu L, Xu J. Zeolitic imidazolate frameworks-8 modified graphene as a green flame retardant for reducing the fire risk of epoxy resin. Polym Adv Technol [Internet]. 2018 Jun 1;29(6):1733–43. Available from: https://doi.org/10.1002/pat.4278 DOI:https://doi.org/10.1002/pat.4278.
[39] Saliba D, Ammar M, Rammal M, Al-Ghoul M, Hmadeh M. Crystal Growth of ZIF-8, ZIF-67, and Their Mixed-Metal Derivatives. J Am Chem Soc [Internet]. 2018 Feb 7;140(5):1812–23. Available from: https://doi.org/10.1021/jacs.7b11589 DOI: 10.1021/jacs.7b11589.
[40] Feng S, Jia X, Yang J, Li Y, Wang S, Song H. One-pot synthesis of core–shell ZIF-8@ZnO porous nanospheres with improved ethanol gas sensing. J Mater Sci Mater Electron [Internet]. 2020;31(24):22534–45. Available from: https://doi.org/10.1007/s10854-020-04764-y DOI:10.1007/s10854-020-04764-y.
[41] Metavarayuth K, Ejegbavwo O, McCarver G, Myrick ML, Makris TM, Vogiatzis KD, et al. Direct Identification of Mixed-Metal Centers in Metal–Organic Frameworks: Cu3(BTC)2 Transmetalated with Rh2+ Ions. J Phys Chem Lett [Internet]. 2020 Oct 1;11(19):8138–44. Available from: https://doi.org/10.1021/acs.jpclett.0c02539 DOI:10.1021/acs.jpclett.0c02539.
[42] Mohanadas D, Mohd Abdah MAA, Azman NHN, Ravoof TBSA, Sulaiman Y. Facile synthesis of PEDOT-rGO/HKUST-1 for high performance symmetrical supercapacitor device. Sci Rep [Internet]. 2021;11(1):11747. Available from: https://doi.org/10.1038/s41598-021-91100-x DOI:10.1038/s41598-021-91100-x.
[43] Sayyad PW, Ingle NN, Bodkhe GA, Deshmukh MA, Patil HK, Shirsat SM, et al. Tuning the properties of Fe-BTC metal-organic frameworks (MOFs) by swift heavy ion (SHI) irradiation. Radiat Eff Defects Solids [Internet]. 2021 Mar 26;176(3–4):274–83. Available from: https://doi.org/10.1080/10420150.2020.1825958 DOI: 10.1080/10420150.2020.1825958.
[44] D. Radhakrishnan, C. Narayana, Guest dependent Brillouin and Raman scattering studies of zeolitic imidazolate framework-8 (ZIF-8) under external pressure. J Chem Phys [Internet]., 6;144(13):134704, Available from: 10 (1063/1) (2016 Apr) 4945013, https://doi.org/10.1063/1.4945013.
[45] Tanaka S, Fujita K, Miyake Y, Miyamoto M, Hasegawa Y, Makino T, et al. Adsorption and Diffusion Phenomena in Crystal Size Engineered ZIF-8 MOF. J Phys Chem C [Internet]. 2015 Dec 24;119(51):28430–9. Available from: https://doi.org/10.1021/acs.jpcc.5b09520 DOI:10.1021/acs.jpcc.5b09520.
[46] Sun H, Jiang H, Kong R, Ren D, Wang D, Tan J, et al. Tuning n-Alkane Adsorption on Mixed-Linker Zeolitic Imidazolate Framework-8-90 via Controllable Ligand Hybridization: Insight into the Confinement from an Energetics Perspective. Ind Eng Chem Res [Internet]. 2019 Jul 24;58(29):13274–83. Available from: https://doi.org/10.1021/acs.iecr.9b00941 DOI:10.1021/acs.iecr.9b00941.
[47] T. Van Tran, D.T.C. Nguyen, T.T. Nguyen, H.T.N. Le, C. Van Nguyen, T.D. Nguyen, Metal-organic framework HKUST-1-based Cu/Cu2O/CuO@ C porous composite: Rapid synthesis and uptake application in antibiotics remediation, J. Water Process Eng. 36 (2020) 101319.
[48] Zhu Z, Wei C, Jiang D, Wu X, Lu M. Design and synthesis of MOF-derived CuO/g-C3N4 composites with octahedral structures as advanced anode materials for asymmetric supercapacitors with high energy and power densities. Mater Adv [Internet]. 2022;3(1):672–81. Available from: https://doi.org/10.1039/D1MA00766A DOI:10.1039/D1MA00766A.
[49] D.-J. Li, S. Lei, Y.-Y. Wang, S. Chen, Y. Kang, Z.-G. Gu, et al., Helical carbon tubes derived from epitaxial Cu-MOF coating on textile for enhanced supercapacitor performance, Dalt Trans. 47 (16) (2018) 5558–5563.
[50] A.D. Salazar-Aguilar, G. Vega, J.A. Casas, S.M. Vega-Díaz, F. Tristan, D. Meneses-Rodríguez, et al., Direct hydroxylation of phenol to dihydroxybenzenes by H2O2 and fe-based metal-organic framework catalyst at room temperature, Catalysts 10 (2) (2020) 172.
[51] A. Yuan, Y. Lu, X. Zhang, Q. Chen, Y. Huang, Two-dimensional iron MOF nanosheet as a highly efficient nanozyme for glucose biosensing, J. Mater. Chem. B 8 (40) (2020) 9295–9303.
[52] Liu J, He J, Wang L, Li R, Chen P, Rao X, et al. NiO-PTA supported on ZIF-8 as a highly effective catalyst for hydrocracking of Jatropha oil. Sci Rep [Internet]. 2016;6(1):23667. Available from: https://doi.org/10.1038/srep23667 DOI: 10.1038/srep23667.
[53] L.G. Devi, K.E. Rajashekhar, A kinetic model based on non-linear regression analysis is proposed for the degradation of phenol under UV/solar light using nitrogen doped TiO2, J. Mol. Catal. A Chem. 334 (1–2) (2011) 65–76.
[54] S. Jeon, K.R. Hurley, J.C. Bischof, C.L. Haynes, C.J. Hogan, Quantifying intra-and extracellular aggregation of iron oxide nanoparticles and its influence on specific absorption rate, Nanoscale 8 (35) (2016) 16053–16064.